geosciences

MDPI

Article

Distinguishing Areas of Cave Collapse: A Case Study Applied to Carter Caves State Resort Park, Kentucky, USA

Ethan W. Conley [1], Eric W. Peterson [1,*], Toby J. Dogwiler [2] and John C. Kostelnick [1]

[1] Department of Geography, Geology, and the Environment, Illinois State University, Normal, IL 61790, USA; ewconle@sandia.gov (E.W.C.)
[2] The School of Earth, Environment, and Sustainability, Missouri State University, Springfield, MO 65897, USA
* Correspondence: ewpeter@ilstu.edu

Abstract

While dissolution dominates the genesis of karst systems, physical erosion processes also play a significant role in their development. Lowering of the water table exposes caves to vadose conditions, reducing roof-supporting buoyancy and potentially leading to catastrophic conduit ceiling failure and cave collapse. The locations and extents of collapse areas are not always identifiable at the landscape surface. High-resolution topographic data derived from LiDAR were used to develop a digital elevation model (DEM) that isolates areas that may have sustained episodes of cave collapse and improves our understanding of past hydrogeological and geomorphological conditions of the system. Cave level delineation from LiDAR data was used to assign elevations to cave entrances. Spatial susceptibility to past collapse was evaluated using a weighted multi-criteria analysis that integrated terrain slope, proximity to mapped cave entrances, and distance to surface streams. Areas identified as having a high likelihood of collapse spatially coincide with cave level contacts and known karst windows and terraces, indicating that this replicated methodology is effective as an initial survey tool for identifying collapse-prone areas in karst landscapes.

Keywords: karst; cave collapse; geospatial analytics

1. Introduction

Karst regions occupy approximately 10–20% of the Earth's terrestrial surface [1–3] and provide drinking water to roughly 10% of the global population [4–6]. Their development is governed primarily by chemical dissolution, especially during early speleogenetic stages, leading to the formation of subsurface flow paths, conduits, and cave networks [7,8]. The geometry and evolution of these systems may further reflect large-scale geomorphic drivers, including incision of major river systems and associated base-level adjustments [9–11]. Incision by river systems controls the regional water table, influencing the elevation at which cave passages develop. When river incision is stagnant for an extended period in karst areas, a cave passage, and subsequently a level, may form in response to the static base-level elevation [3,12].

During periods of constant base level, large horizontal phreatic passages develop at the base level elevations; these passages represent a cave level [13–16]. The upper and lower elevation bounds of cave levels are commonly marked by a shift from predominant horizontal flow to vertical flow. The observed transition reflects episodic lowering of the local base level driven by regional river incision [17]. For instance, cave levels at Mammoth

Check for updates

Academic Editor: Mario Parise

Received: 6 January 2026
Revised: 12 February 2026
Accepted: 20 February 2026
Published: 1 March 2026

Copyright: © 2026 by the authors. Licensee MDPI, Basel, Switzerland. This article is an open access article distributed under the terms and conditions of the Creative Commons Attribution (CC BY) license.

Cave (Kentucky) developed in response to phases of fluvial entrenchment associated with rivers in the Interior Low Plateaus, themselves influenced by the evolution of the Ohio River under continental- to global-scale glacioeustatic forcing [18,19]. The development of discrete cave levels is likewise associated with fluvial terraces—relatively flat geomorphic surfaces that record prolonged intervals of base-level stability [20,21].

Although chemical dissolution is fundamental to the early development of karst systems [1,5,22], mechanical erosion also contributes to their evolution and should not be overlooked [1,23–27]. The corresponding lowering of the water table produces vadose conditions and a loss of roof-supporting buoyancy within a cave [28]. While progressive weathering and dissolution processes, along with the development and enlargement of structural discontinuities, are primarily responsible for long-term rock strength deterioration in karst systems [29,30], reductions in buoyant support can act as a triggering mechanism that promotes ceiling instability and collapse in already weakened cave roofs. Karstic collapse is not limited to within a cave passage and the collapse may extend to the land surface, developing a karst window [3,31,32].

Karst windows are significant geomorphic features in regions that have undergone episodes of cave passage collapse [33,34]. Collapsed areas tend to be confined between vertical bedrock walls and may coincide with the presence of large, angular debris. Ranging in size from a few meters to several hundred meters, karst windows often expose subterranean streams within the zones of collapse [34]. Regardless of the presence of streamflow, valley profiles that align with cave passages offer valuable insight into areas where cave passage collapse has previously occurred [35,36]. Zones of cave collapse are not consistently apparent at the surface. To better characterize catastrophic rock failure and its influence on karst system evolution, it is essential to identify and document locations of previous collapse. Expanding the number of documented collapse sites will also support future efforts to develop models of major river system incision.

The increasing resolution of topographic data, coupled with improvements in geospatial analysis tools, provides novel opportunities to investigate karst collapse features with greater precision and to reinterpret their formation processes within a broader geomorphic context.

Using a compiled database of mapped cave entrance locations within and surrounding Carter Caves State Resort Park (CCSRP), Jacoby et al. [37] delineated cave levels based on a digital elevation model (DEM) with a 10 m horizontal resolution and a $\pm$0.36 m vertical accuracy. Following a similar workflow, this study applies geospatial analysis using updated LiDAR-derived topographic data to delineate cave levels and identify areas with a high probability of past cave passage collapse.

Probabilities of cave collapse were assessed through a weighted overlay analysis incorporating slope (percentage), distance to the nearest cave entrance, and distance to the nearest stream channel. We hypothesize that areas with the highest probability of past cave collapse will spatially correspond to the elevations of the delineated cave levels. Subsequently, cave level elevations were recalculated using the LiDAR DEM following the adapted workflow. These data were then used to inform the spatial identification of previously collapsed areas within the CCSRP region.

2. Materials and Methods

2.1. Site Description

Located within the northwest-central portion of Carter County, Kentucky (USA) (Figure 1), the karst areaencompassing Carter Caves State Resort Park (CCSRP) covers approximately 106 km^2 of deeply incised valley terrain ranging in elevations from 200 m above mean sea level to 345 m, which is characteristic of the Cumberland Plateau [38].

CCSRP has been the focus of numerous studies [36–45]; readers are directed to those works for detailed descriptions of the area. Here we provide a summary of the relevant geology.

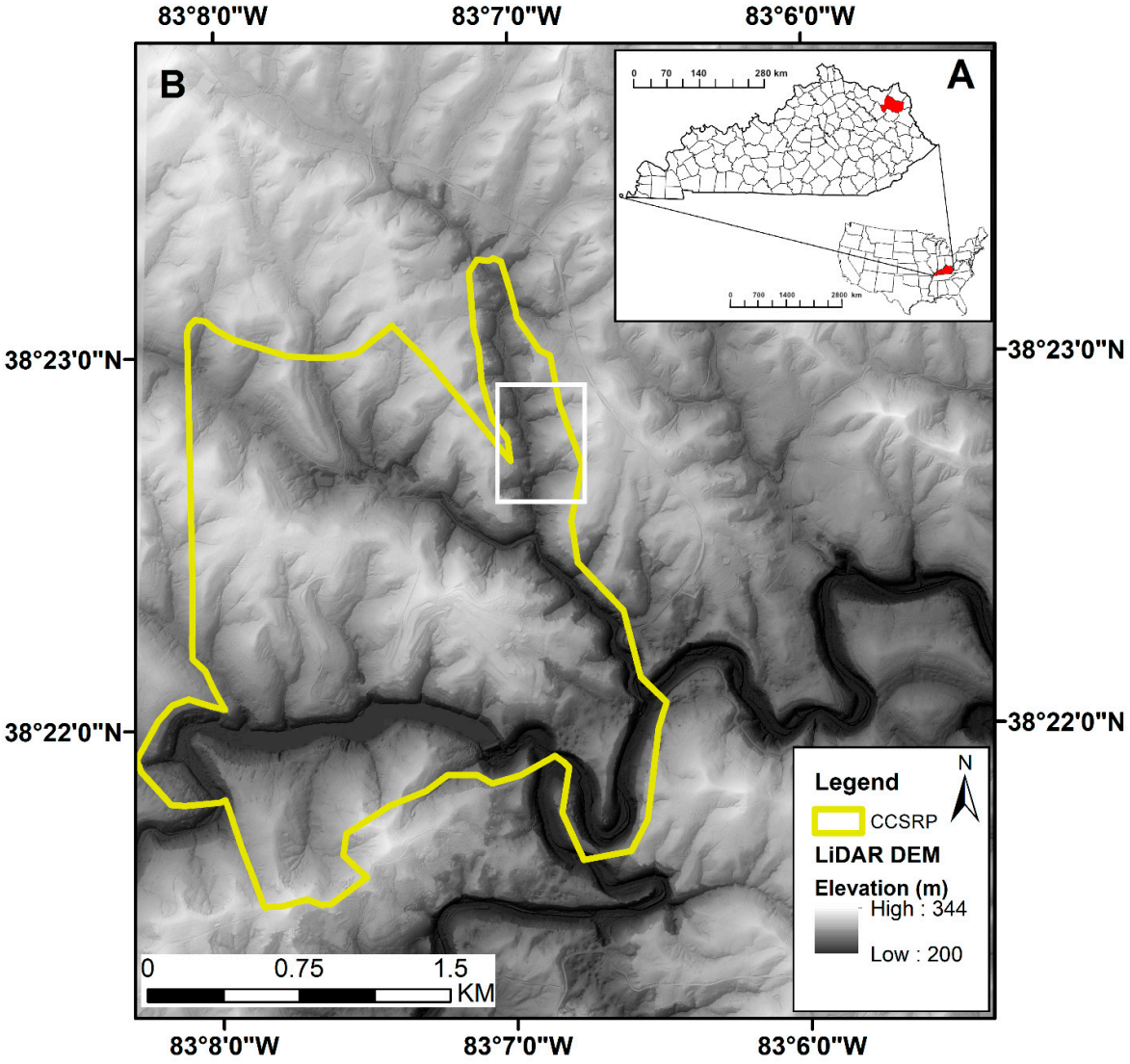

Figure 1. (**A**) Carter Caves State Resort Park (CCSRP) is located in northeastern Kentucky, USA. (**B**) The park boundary is shown by the yellow outline. The white box highlights the lower portion of Horn Hollow, including the Horn Hollow karst window, the lower Horn Hollow entrance, and the upper Laurel Cave entrance presented in Figure 8.

The bedrock framework of the study area consists of Mississippian- to Pennsylvanian-aged siliciclastic and carbonate units (Figure 2). The oldest unit exposed near CCSRP is the Mississippian Borden Formation, a shale-dominated succession that forms the stream bedrock, controls local base level, and restricts further vertical incision [38,40]. Overlying the Borden, the Mississippian Newman Formation represents the principal cave-forming unit within the park. This carbonate unit is approximately 25 m thick in the study area and is extensively jointed, promoting focused recharge and enhanced dissolution of the bedrock [38,39]. A gentle regional dip of roughly 2° toward the east-southeast has facilitated the development of laterally extensive, near-horizontal cave passages [41,42]. Capping the sequence is the Pennsylvanian Pennington Formation, a resistant sandstone unit approximately 100 m thick that overlies the Newman Formation and acts as a protective caprock across much of CCSRP [38,40]. Within the study area, the Newman–Pennington contact occurs at an elevation of approximately 273 m.

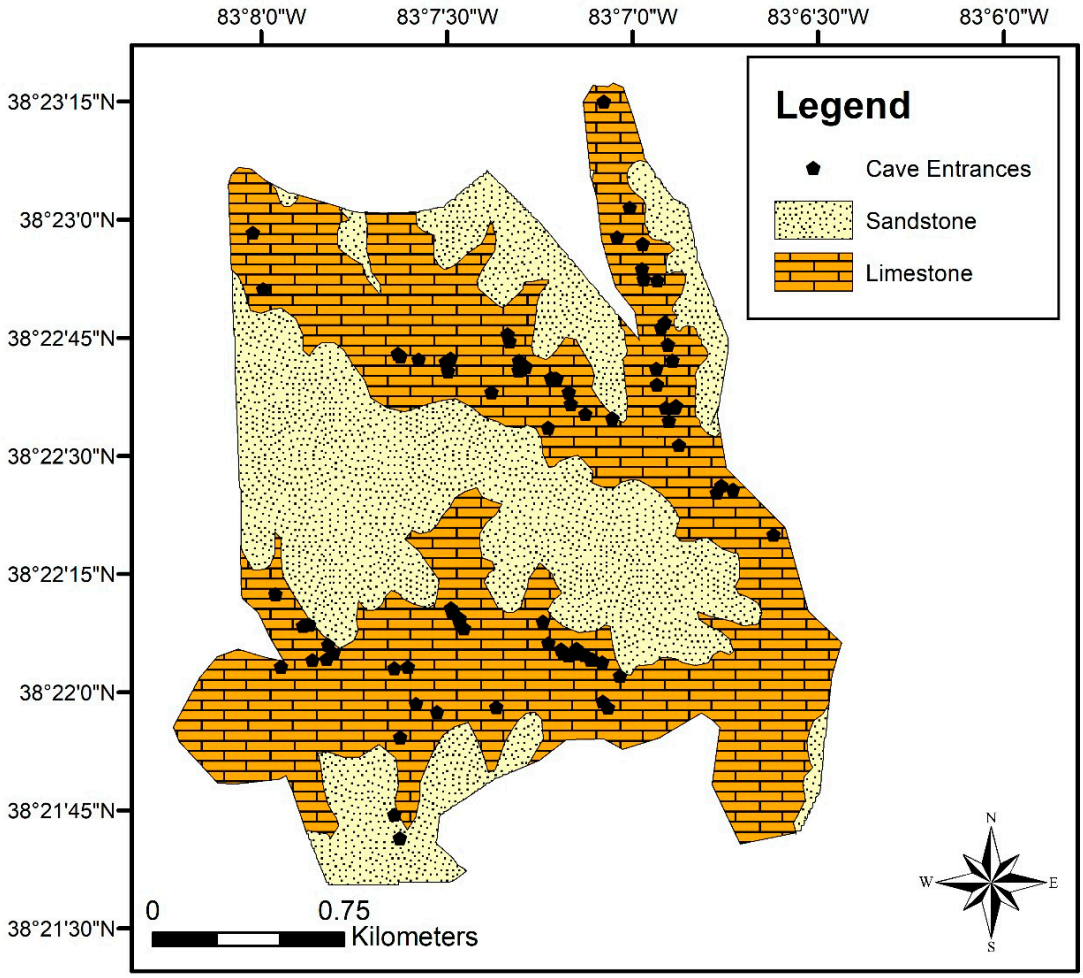

Figure 2. Distribution of the sandstone and limestone within CCSRP, with the locations of cave entrances (unpublished WUSS data).

Several karst features directly relevant to this investigation have been documented at CCSRP. For example, ref. [45] showed that stream reaches developed in limestone exhibit higher steepness index values than those incised into sandstone, suggesting that the limestone segments are not presently in erosional equilibrium. Karst windows are present within CCSRP. Within lower Horn Hollow (Figure 1), a karst window is present between two cave entrances [38,39].

2.2. LiDAR Data

Twelve LAZ files containing compressed LiDAR point cloud data were obtained from the KGS GeoPortal [46]. The dataset provides an average horizontal resolution of approximately 0.68 m and a vertical accuracy of ±15 cm. Because LAZ format is not directly supported in ArcGIS (ArcMap or ArcGIS Pro) (Esri, Redlands, CA, USA), the files were decompressed to LAS format using LASzip (v3.4.3). The resulting LAS files were imported to generate point feature information, from which mean point spacing was calculated using attribute table statistics. This spacing value was then used to construct a terrain dataset from the multipoint data, which was subsequently converted to a raster with 0.68 m horizontal resolution to enable spatial analysis of surface elevation.

2.3. Cave Levels

Elevations of cave levels were determined following the methodology utilized by [37], which used a Jenks Natural Breaks classification method [47]. Using data from an unpub-

lished cave dataset provided by Wittenberg University Speleological Society (WUSS), the latitude and longitude coordinates of the individual cave entrances were plotted in the GIS (ArcMap 10.8.2). Previous work [36,37] verified the latitude and longitude coordinates of select cave entrances to a submeter accuracy using a Trimble GeoExplorerXT (dGPS) (Trimble, Westminster, CO, USA). Elevations for the cave entrances were extracted from the LiDAR DEM. Although the entrances themselves do not serve as the level, the entrances used in this work align with the horizontal cave passages and were used as a proxy for passage elevation. While pit entrances are present within the area, no pit entrances were used to identify the levels.

2.4. Digitization and Euclidean Distance

A stream network was delineated directly from the LiDAR-derived raster by calculating flow direction and flow accumulation grids. This approach was selected instead of relying on existing hydrographic datasets (e.g., the USGS National Hydrography Dataset) to ensure that the extracted drainage network was fully consistent with the LiDAR DEM. Before computing these flow metrics, surface depressions were filled to remove artificial sinks introduced during raster processing. However, depression filling in karst terrain requires careful consideration, as many pits and closed depressions represent genuine geomorphic features—such as sinkholes or collapse structures—rather than data artifacts. In non-karst areas, depressions are interpreted as the result of an error in the DEM, which may not be true for karst systems where sinkholes and swallets create depressions. As this study was not focused on these small pits, the decision to fill sinks was made strictly to generate a stream network representative of surface drainage conditions. Without filling depressions, closed features present in the DEM would artificially trap flow, preventing downstream routing and interrupting the continuity of the derived channel network [43].

2.5. Weighted Overlay

To identify areas within CCSRP that have likely undergone episodes of cave collapse, raster layers representing topographic slope, distance to cave entrances, and distance to streams were generated and integrated using a weighted overlay approach (Figure 3). Each layer was assigned a percentage weight reflecting its relative contribution to the final collapse probability, reported in the order slope%_cave%_stream%.

Because distance to streams and cave entrances must be represented in a format suitable for multi-criteria analysis, both datasets were converted to ordinal scales. Euclidean Distance operations were applied to calculate straight-line distances from each raster cell to the nearest stream and cave entrance. The resulting distance rasters were then reclassified on a scale of 1 to 10, where cells farthest from a given feature were assigned a value of 1 and those closest were assigned a value of 10 (Table 1). Similarly, LiDAR-derived slope was reclassified to an ordinal range of 1 (lowest slope) to 10 (steepest slope) (Figure 3A; Table 1). All derived and reclassified rasters retained the original LiDAR cell resolution of 0.68 m $\times$ 0.68 m.

Slope was assigned the highest weight in all weighted distributions because collapse features, such as dolines, are characterized by vertical, steep-sided walls [34,48]. Solution dolines are formed through a gradual process of sagging or settling of overlying materials and do not produce steep-sided walls associated with collapse dolines [7,49]. Proximity to known cave entrances was assigned the second-highest weight, as collapse within a cave system often preserves an identifiable entrance even when internal passages fail. In contrast, distance to streams received the lowest weight. Although fluvial processes are fundamental to speleogenesis, surface streams may develop independently of cave

formation or correspond to lower cave levels not directly associated with the collapse features of interest.

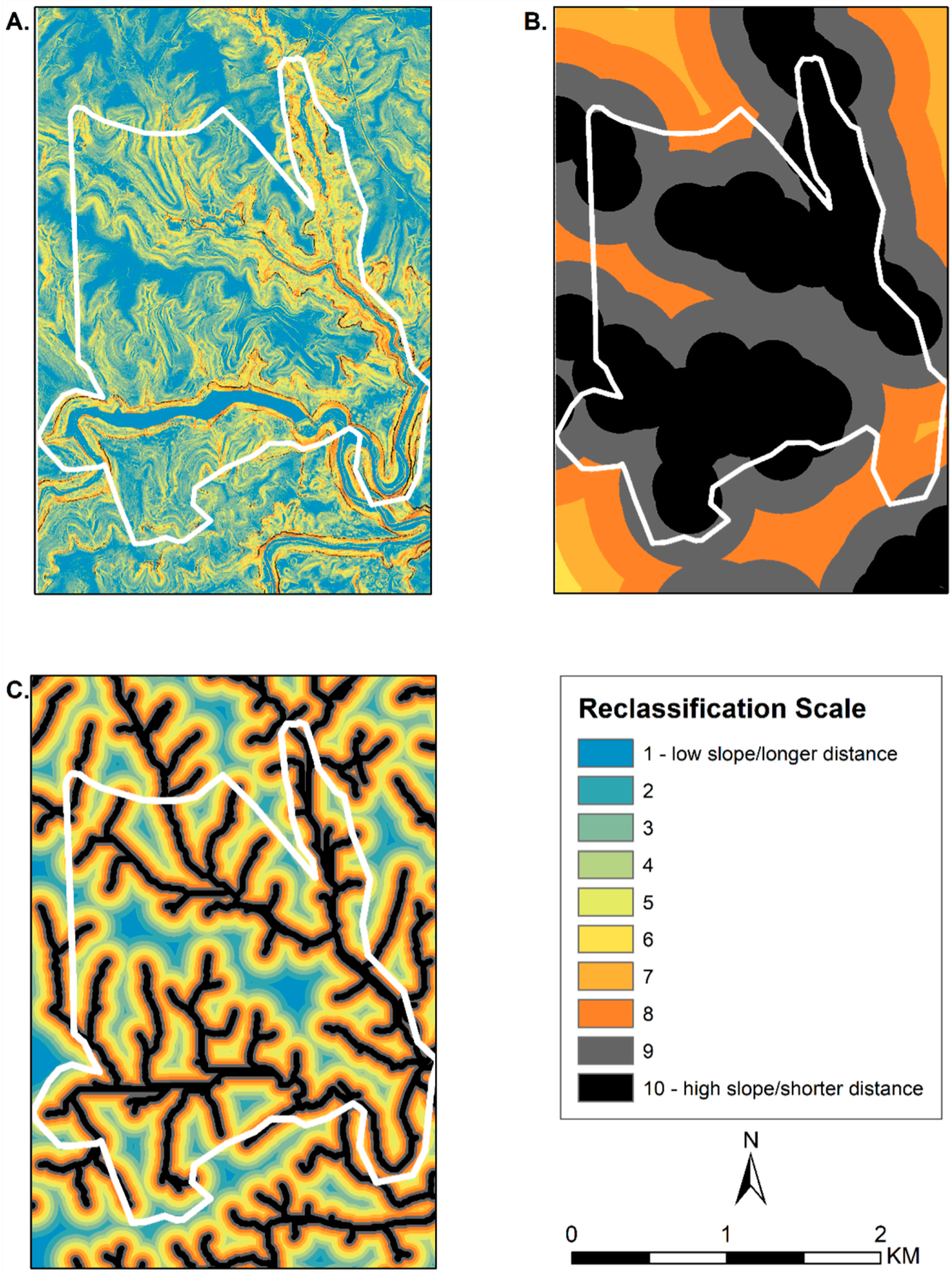

Figure 3. (**A**) Reclassified topographic slope raster, where a value of 1 represents the lowest slopes and 10 represents the steepest slopes. (**B**) Reclassified distance-to-cave raster, with 1 assigned to cells farthest from a cave entrance and 10 assigned to those closest. (**C**) Reclassified distance-to-stream raster, where 1 corresponds to the greatest distance from a stream and 10 to the shortest distance. For all three layers, lower values (1) contribute the least influence and higher values (10) contribute the greatest influence in the weighted overlay analysis. The CCSRP park boundary is shown by the white outline.

Table 1. Parameter values associated with the ranks of reclassified input layers.

Rank	Distance to Stream (m)	Parameter Distance to Cave Entrance (m)	Slope (%)
1	1112–727	2841–2395	5.1–0
2	727–600	2395–2050	9.5–5.1
3	600–512	2050–1727	14.0–9.5
4	512–438	1727–1437	18.4–14.0
5	438–368	1437–1170	23.5–18.4
6	368–298	1170–925	29.7–23.5
7	298–223	925–691	37.5–29.7
8	223–149	691–457	48.5–37.5
9	149–70	457–230	63.5–48.5
10	70–0	230–0	87–63.5

Because the spatial extent of each input layer depended on data availability and processing boundaries, their geographic coverage was not identical. Consequently, only weighted overlay values ranging from 2 to 10 were present within the defined study area. Cells assigned a probability value of 1 occurred outside the final analysis extent and were removed during clipping to the study boundary.

To determine the best weight combination for the three parameters, a visual comparison was conducted to assess the importance and significance that each individual parameter has on the resulting output. Weighting scenarios varied from 90%_5%_5% to 34%_33%_33%. After generating the full set of weighted overlays using these different percentage combinations, the number of cells within each probability class (1–10, where 1 represents the lowest likelihood and 10 the highest) was calculated and compared across scenarios.

3. Results and Discussion

3.1. Cave Entrance Elevations and Level Designations

To assess the differences in elevation values obtained from the 10 m DEM as compared to the LiDAR DEM (Figure 4), the 10 m cave entrance elevations were subtracted from the LiDAR cave entrance elevations. The differences between the elevation for the 117 cave entrances ranged from −21.6 m to 15.3 m, with a mean difference of −0.73 m. The results indicate the 10 m cave entrance elevations were, on average, higher than the LiDAR cave entrance elevations.

Using the LiDAR-derived cave opening elevations, four cave levels were identified with elevation breaks at 216 m, 233 m, 244 m, and 255 m (Figure 5). The elevation for each break was higher than those reported by [37] for the 10 m DEM data. The LiDAR-generated elevations have placed all but one cave within the limestone units. Although caves can develop in siliciclastic units, such occurrences are uncommon within the formations present in this study area. In earlier work [37], siliciclastic cave entrances introduced elevation uncertainties that affected cave-level interpretations. The higher-resolution LiDAR dataset substantially reduced this source of error. In particular, the steep contact between the Newman and Pennington Formations is better resolved in the LiDAR DEM, which more accurately captures subtle elevation differences across sharp slopes. At a regional scale, a comparable four-level cave framework has been proposed for the geologically analogous Mammoth Cave system [19,50].

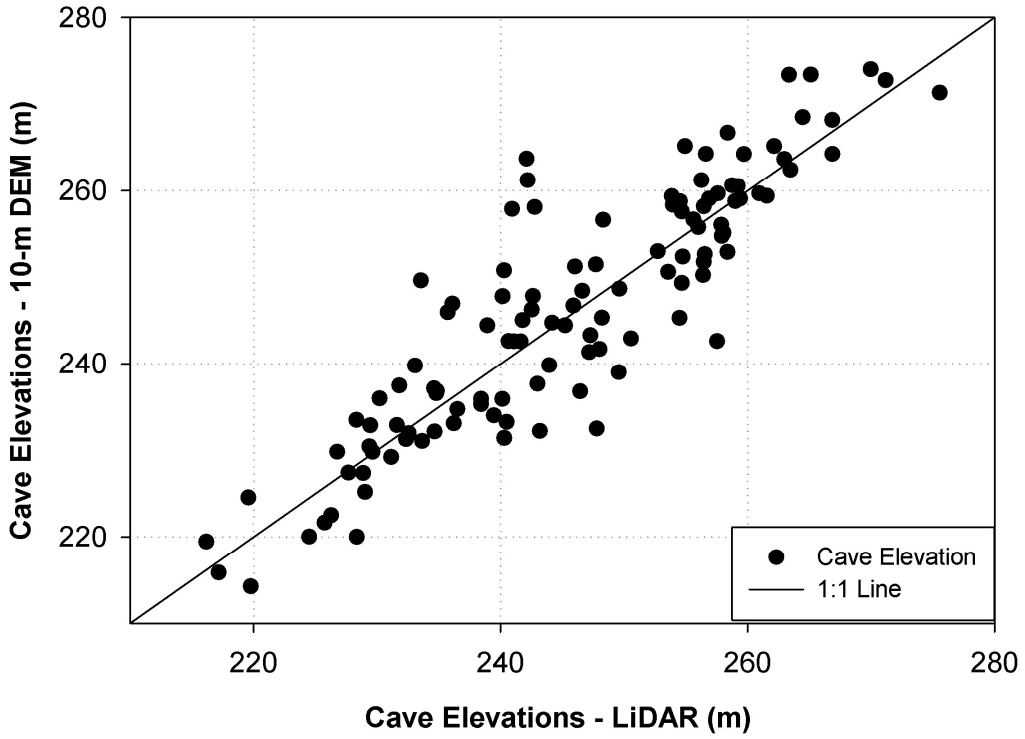

Figure 4. Comparison of cave entrance elevations derived from LiDAR data and a 10 m DEM [37]. On average, elevations extracted from the LiDAR dataset are 0.73 m lower than those obtained from the 10 m DEM. The black line denotes the 1:1 reference line.

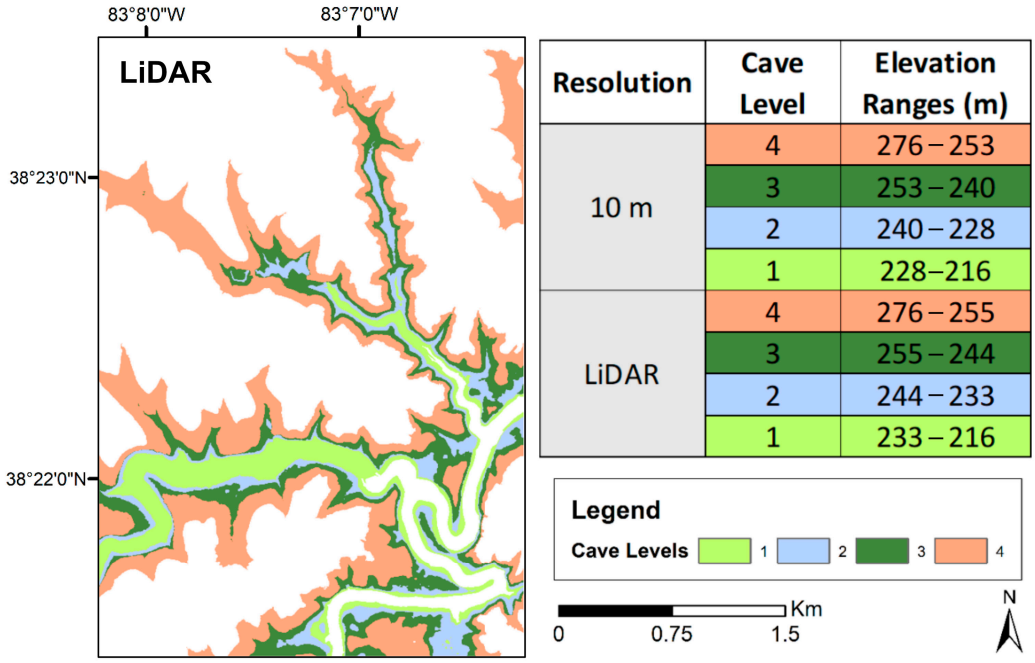

Figure 5. Spatial distribution of the cave levels derived using Jenks Natural Breaks statistical methodology for LiDAR DEM data. Statistics are provided for both the LiDAR data and the previously used 10 m data [37].

3.2. Evaluation of Weighted Overlay Scenarios

To differentiate areas that have experienced past collapse, limiting the number of cells associated with the higher probabilities narrows the possibilities and makes for a more precise and accurate output. Using a sensitivity analysis to optimize the results, we aimed to achieve between 1% and 2% of the total number of cells to be included in probabilities

9 and 10 combined (areas considered to be cave collapse). When results fell outside of the 1% to 2% range, the higher probabilities either mirrored slope inputs or became spatially homogenized. The weighting scheme satisfied the predefined area threshold (between 1% and 2%); however, it was excluded to avoid disproportionately emphasizing slope in the final output. Based on evaluation of the remaining scenarios, a slope weight between 75% and 65% was identified as an appropriate balance. Within this range, variations in weighting produced minimal differences in the spatial distribution of high-probability cells, indicating low sensitivity to small adjustments in slope percentage. The 70%_20%_10% configuration was ultimately selected, as it preserved slope as the primary controlling variable while still effectively considering the weights for both distance from cave entrances and from streams (Figure 6).

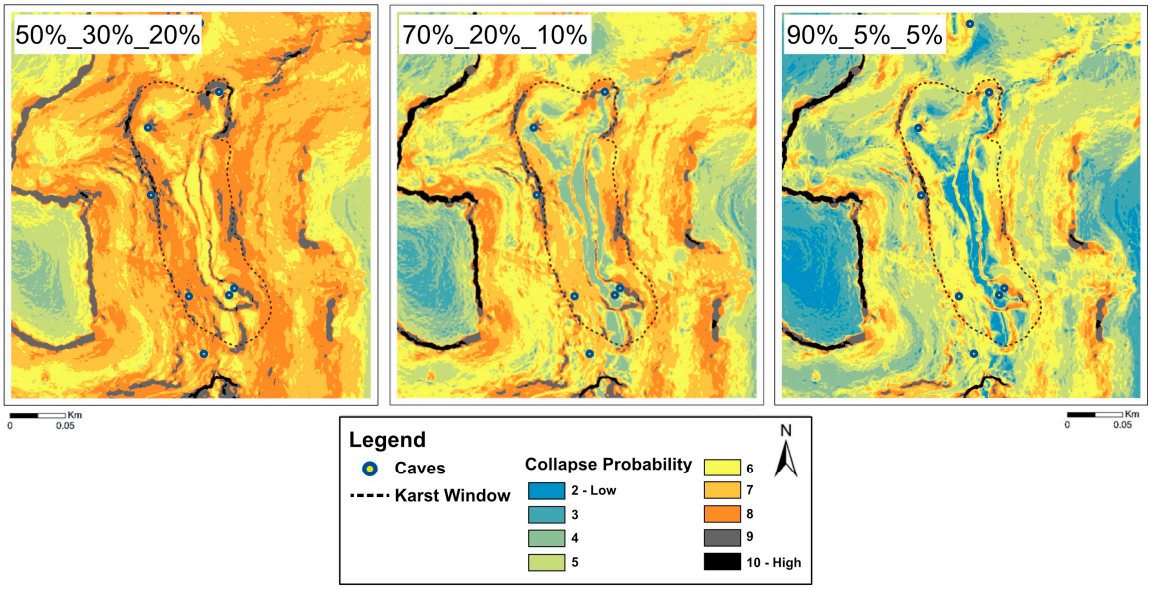

Figure 6. This figure presents a visual comparison of three weighted overlay combinations: the selected layer with 70% slope, 20% caves, and 10% other features. For comparison, the other two weight combinations shown are 50%, 30%, 20% and 90%, 5%, 5%. The analysis indicates that combinations with lower slopes than 70% tend to diminish the significance of slope, while those with higher slopes than 70% skew the results in favor of slope. Based on these observations, a slope weight between 65% and 75% is deemed optimal.

The weighted overlay (using 70%_20%_10% distribution) for CCSRP provides a clear distinction between areas of high and low probability of past collapse (Figure 7). Several features indicate that the use of weighted overlays may be an effective methodology for cave collapse identification, including karst windows, contacts between lithologies, terraces between areas of high probability, and the visual correlation between high probabilities of collapse and contacts between known cave levels formulated previously in this study.

The generated probabilities identify karst windows in CCSRP (Figures 8 and 9). The first example is a karst window in lower Horn Hollow (Figure 8); the window has steep walls and a lack of surficial drainage paths, indicating that water entering this valley must exit through an existing cave passage. While the boundary of the window was not as well-defined by the maximum probability as other reaches, the extent of the window aligns with cells designated with the highest probability values. The second example in CCSRP consists of an interconnected series of karst windows (Figure 9). Figure 9 provides evidence for a potential flow path that alternates between surface and subsurface flow. Locations where flow enters or exits the subsurface correspond to areas of elevated probability of

past collapse. The regularity of these features supports a linked and internally consistent cave system.

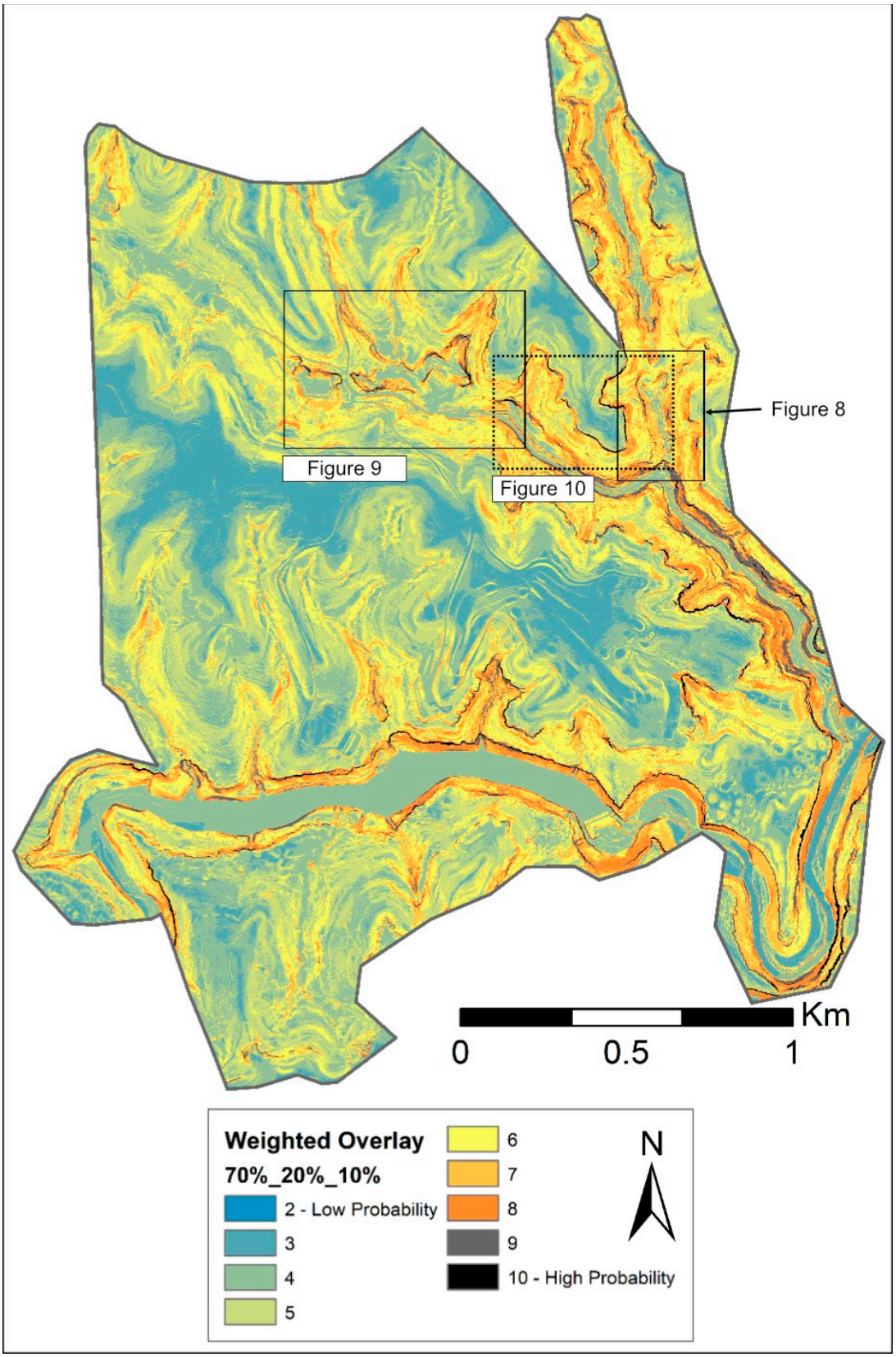

Figure 7. Weighted overlay of 70% slope, 20% caves, and 10% streams displaying probabilities of past cave collapses in and around CCSRP. Black boxes indicate extents for Figures 8–10.

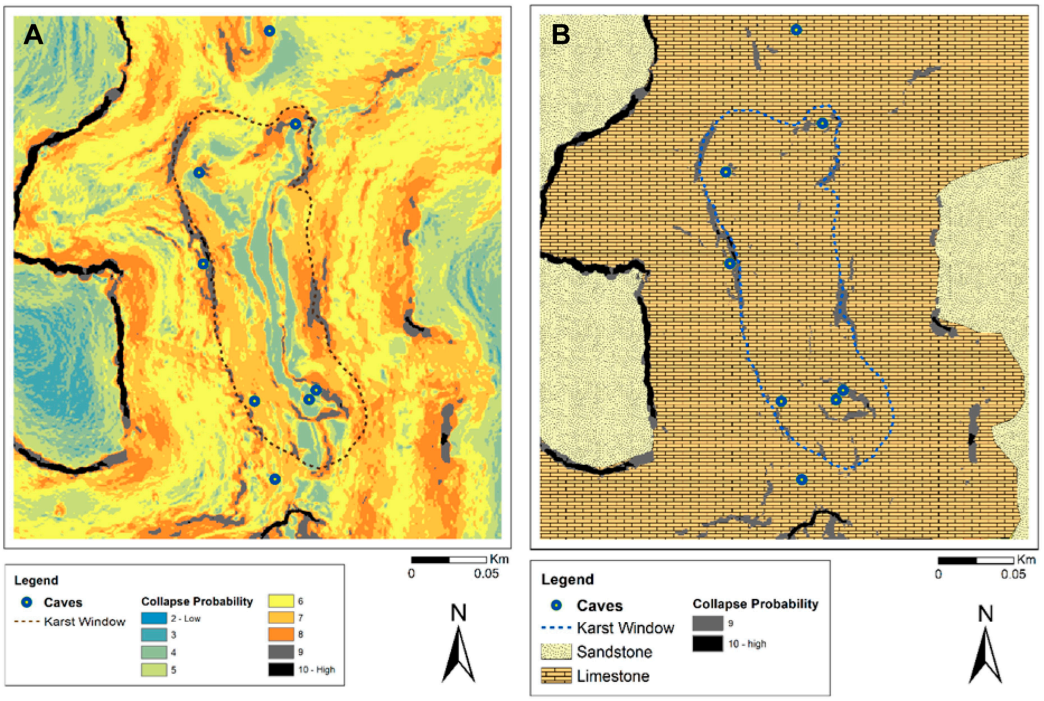

Figure 8. (**A**) Collapse probability map for the karst window situated between the lower Horn Hollow entrance and the upper Laurel Cave entrance, outlined by the dashed brown line. Elevated probability values within the window delineate steep faces that have been previously identified and interpreted as collapse features. (**B**) Location of collapse probabilities designated 9 and 10 for the Horn Hollow karst window.

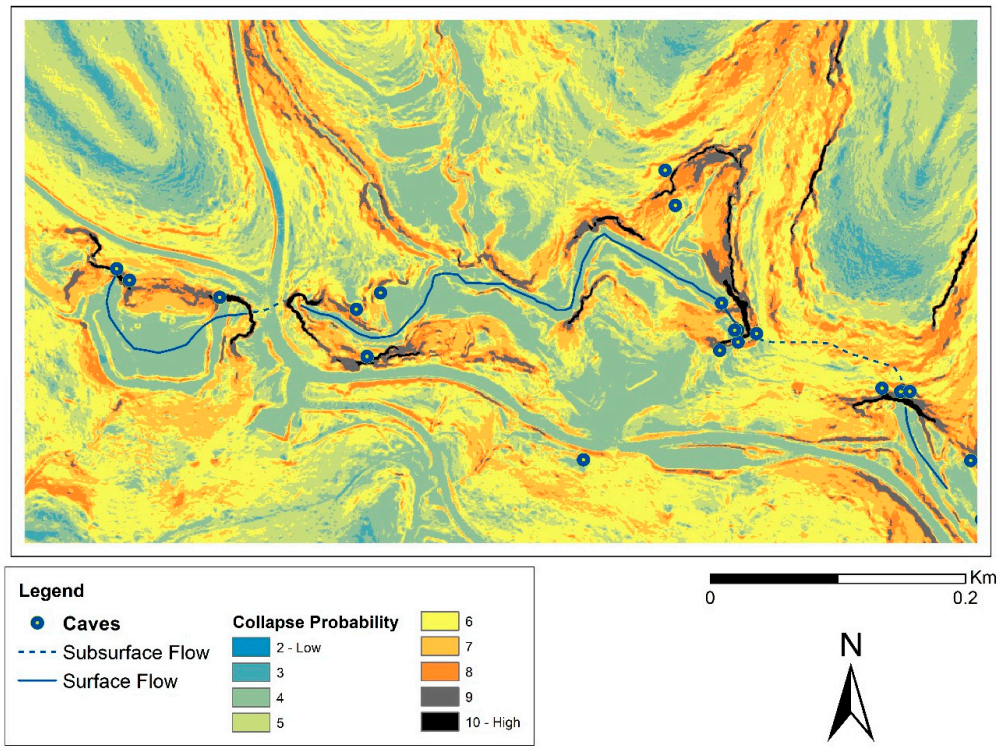

Figure 9. A sequence of karst windows located in the western portion of CCSRP. The blue line illustrates a conceptual pathway of subsurface connectivity. It is possible that this route was once entirely confined below ground, with subsequent ceiling collapse exposing segments of the former conduit as isolated karst windows.

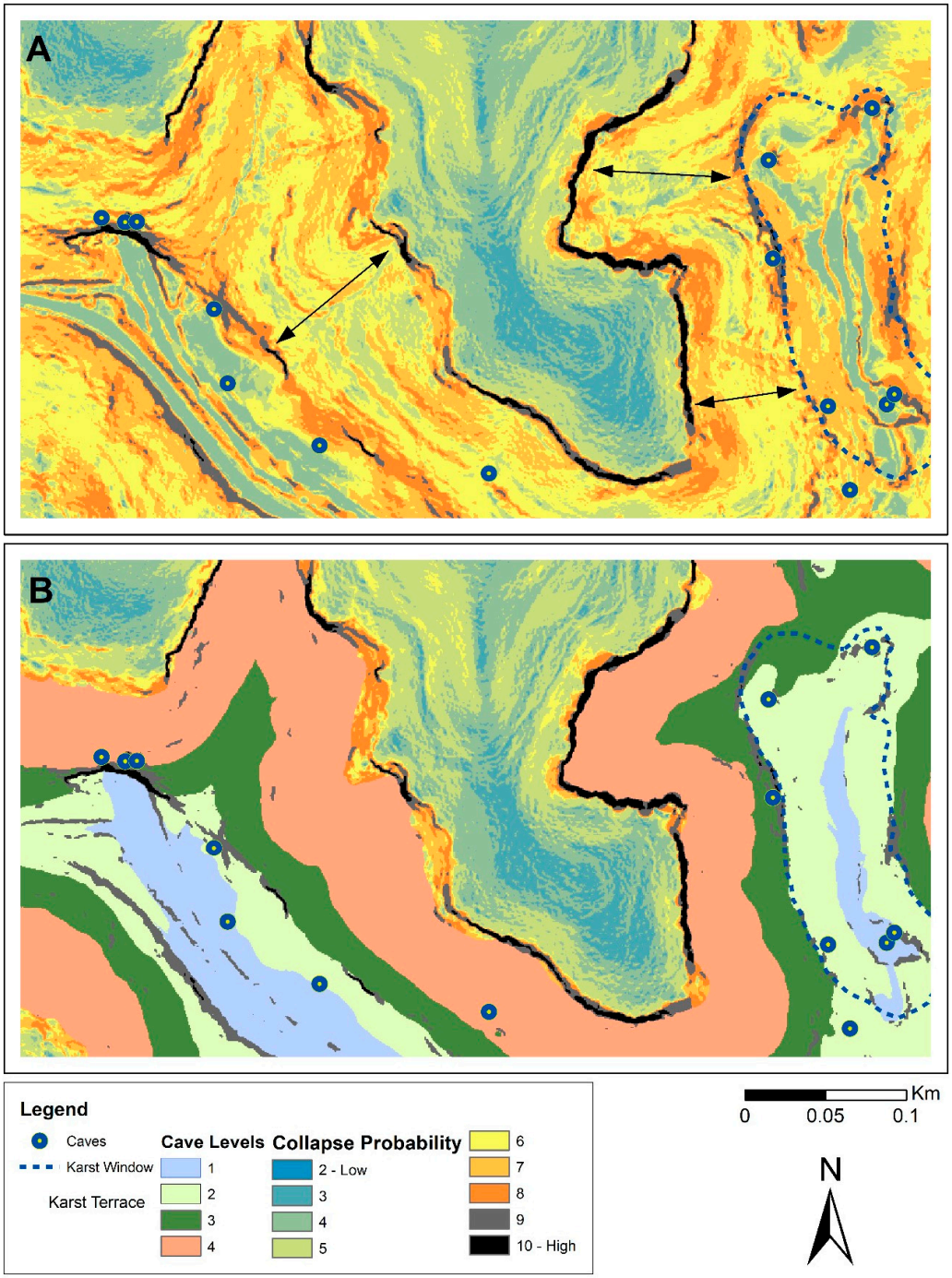

Figure 10. (**A**) Karst terraces occurring between zones of high collapse probability, indicated by arrows. (**B**) Apparent spatial relationship between high-probability collapse areas and mapped contacts between distinct cave levels.

Contacts between carbonate and non-carbonate lithologies in karst systems often yield identifiable fluviokarst features [51,52]. Limestone responds to both physical and chemical weathering, whereas sandstone erodes through physical weathering processes. Water flowing from the sandstone to the limestone is solutionally aggressive because it has not yet interacted with the carbonate bedrock [53]. The aggressive water (or carbonic acid) dissolves the limestone, creating a greater state of disequilibrium. The contact between the limestone and sandstone in CCSRP is marked by a steep contact, which is well-defined by the weighted overlay (Figure 8B). While the contact does not mark an area of collapse,

its identification by the weighted overlay speaks to the utility of the method to identify karst features.

Karst terraces are commonly associated with intervals of regional base-level stability [20,21]. At CCSRP, the spatial distribution of isolated collapse zones is separated by surfaces interpreted as karst terraces. The cave levels previously identified within the park appear to correspond directly to these terrace elevations. In Horn Hollow specifically, distinct bands of cells classified as high collapse probability are divided by intervening zones of lower probability, further supporting this interpretation (Figure 10A). The high probabilities align with the boundaries of these cave levels, suggesting that cave collapse may preferentially occur at the boundaries between cave levels (Figure 10B). It could additionally be interpreted as an indication of several episodes of collapse. As the water table drops, only a subset of cave levels may be exposed to vadose conditions, resulting in collapse at those elevations due to the loss of buoyant support. As base level changes through time, additional cave levels within the same geographic areas may subsequently be exposed and undergo collapse. This process may result in multiple collapse events at different cave levels within the same geographic areas, both at CCSRP and in other systems with similar hydrogeologic genesis.

This approach is not limited to a single study area. Any region exhibiting karst terrain and supported by adequate spatial data, such as mapped cave entrance locations, can be evaluated using this framework to delineate cave levels and identify potential collapse features. Other studies, such as [54], offer promising and novel approaches for identifying karstic collapse features; however, these methods are spatially constrained by site-specific data acquisition requirements. Results from this study suggest that geospatial analyses provide an effective first-order framework for identifying collapse-prone areas, which can be further refined through incorporation of rock strength, structural, and stability analyses as proposed in previous karst and sinkhole studies [29,30]. Based on the results of this paper, where geospatial data with resolutions of 10 m or better are available, cave levels and isolated areas of cave collapse can be identified. To further test the effectiveness of this methodology, the study could be duplicated at sites similar to CCSRP like Mammoth Cave or the Cumberland Plateau.

4. Conclusions

The methodology applied in this study is inherently exploratory and designed as a first-order spatial assessment rather than a deterministic predictive model. Nevertheless, the weighted overlay outputs consistently delineate zones of elevated collapse probability that correspond with independently mapped karst windows and previously identified collapse features. These high-probability areas also align with LiDAR-derived cave-level elevations and clearly track the pronounced lithologic transition between the Newman limestone and the overlying Pennington sandstone, reinforcing the geomorphic and structural controls for collapse development.

In contrast, low-probability classifications cluster on relatively flat cave terraces and in areas dominated by siliciclastic lithology, where dissolution-driven void formation is less prevalent. The coherence between modeled probability patterns and established geomorphic and stratigraphic relationships provides confidence that the approach is capturing meaningful landscape controls rather than producing arbitrary spatial artifacts.

Taken together, these results suggest that weighted overlay analysis, when supported by high-resolution LiDAR data and reliable cave inventories, represents a preliminary tool for identifying potential collapse zones in karst terrain. While further validation through field verification and mechanical stability assessments would strengthen the predictive capability, the framework offers a transferable and efficient screening method.

Application to geologically comparable systems, such as Mammoth Cave or the Cumberland Plateau, would provide an opportunity to test reproducibility and evaluate broader regional applicability.

Author Contributions: Conceptualization, E.W.C., E.W.P., T.J.D. and J.C.K.; methodology, E.W.C. and J.C.K.; validation, E.W.C., E.W.P. and T.J.D.; formal analysis, E.W.C.; investigation, E.W.C. and E.W.P.; resources, J.C.K.; writing—original draft preparation, E.W.C. and E.W.P.; writing—review and editing, E.W.C., E.W.P., T.J.D. and J.C.K.; visualization, E.W.C.; supervision, E.W.P. All authors have read and agreed to the published version of the manuscript.

Funding: This research received no external funding.

Data Availability Statement: The data used in this study include publicly available GIS layers obtained from the Kentucky Geological Survey and third-party cave database records provided by the Western Kentucky University Speleological Society (WUSS). Restrictions apply to the availability of the cave database data, which were obtained from WUSS and are not publicly available. Access to these data may be possible with the permission of WUSS.

Acknowledgments: This manuscript is derived in part from the first author's Master's thesis titled "Isolating Locations of Potential Episodes of Cave Collapse and Their Relationship to Cave Level Development through Major River System Incisions" completed at Illinois State University (2021). The thesis is available at https://ir.library.illinoisstate.edu/etd/1431/ as of 12 February 2026. The authors thank the Wittenberg University Speleological Society (WUSS) for providing access to the karst database. No Funding was received for this work.

Conflicts of Interest: The authors declare no conflicts of interest.

References

1. Palmer, A.N. Origin and morphology of limestone caves. *Geol. Soc. Am. Bull.* **1991**, *103*, 1–21. [CrossRef]
2. Goldscheider, N.; Chen, Z.; Auler, A.S.; Bakalowicz, M.; Broda, S.; Drew, D.; Hartmann, J.; Jiang, G.; Moosdorf, N.; Stevanovic, Z.; et al. Global distribution of carbonate rocks and karst water resources. *Hydrogeol. J.* **2020**, *28*, 1661–1677. [CrossRef]
3. Zerga, B. Karst topography: Formation, processes, characteristics, landforms, degradation and restoration: A systematic review. *Watershed Ecol. Environ.* **2024**, *6*, 252–269. [CrossRef]
4. Zhang, J.; Liesch, T.; Chen, Z.; Goldscheider, N. Global analysis of land-use changes in karst areas and the implications for water resources. *Hydrogeol. J.* **2023**, *31*, 1197–1208. [CrossRef]
5. Çallı, K.; Chiogna, G.; Bittner, D.; Sivelle, V.; Labat, D.; Richieri, B.; Çallı, S.; Hartmann, A. Karst water resources in a changing world: Review of solute transport modeling approaches. *Rev. Geophys.* **2025**, *63*, e2023RG000811. [CrossRef]
6. Stevanović, Z. Karst waters in potable water supply: A global scale overview. *Environ. Earth Sci.* **2019**, *78*, 662. [CrossRef]
7. Jennings, J. *Karst Geomorphology*; Basil Blackwell Inc.: New York, NY, USA, 1985; p. 293.
8. Xiaojuan, Q.; Baoling, L.; Kai, L.; Xinyu, C.; Wenjin, Y. Hydrochemical characteristic and karst development in typical karst spring area, Northern China. *Front. Environ. Sci.* **2025**, *12*, 1494730. [CrossRef]
9. Anthony, D.M.; Granger, D.E. A new chronology for the age of Appalachian erosional surfaces determined by cosmogenic nuclides in cave sediments. *Earth Surf. Process. Landf. J. Br. Geomorphol. Res. Group* **2007**, *32*, 874–887. [CrossRef]
10. Springer, G.S.; Poston, H.A.; Hardt, B.; Rowe, H.D. Groundwater lowering and stream incision rates in the Central Appalachian Mountains of West Virginia, USA. *Int. J. Speleol.* **2015**, *44*, 10. [CrossRef]
11. Pennos, C.; Skoglund, R.Ø.; Thorvik, M.; Lauritzen, S.E. Glacial valley erosion controls on subsurface hydrology: Speleogenesis of Stortuvhola cave, sub-Arctic Norway. *Geomorphology* **2026**, *498*, 110191. [CrossRef]
12. Palmer, A.N. *Cave Geology*; Cave Books: Dayton, OH, USA, 2007.
13. Palmer, A.N. Cave levels and their interpretation. *Natl. Speleol. Soc. Bull.* **1987**, *49*, 50–66.
14. Harmand, D.; Adamson, K.; Rixhon, G.; Jaillet, S.; Losson, B.; Devos, A.; Hez, G.; Calvet, M.; Audra, P. Relationships between fluvial evolution and karstification related to climatic, tectonic and eustatic forcing in temperate regions. *Quat. Sci. Rev.* **2017**, *166*, 38–56. [CrossRef]
15. Columbu, A.; Sauro, F.; Lundberg, J.; Drysdale, R.; De Waele, J. Palaeoenvironmental changes recorded by speleothems of the southern Alps (Piani Eterni, Belluno, Italy) during four interglacial to glacial climate transitions. *Quat. Sci. Rev.* **2018**, *197*, 319–335. [CrossRef]

16. Zhai, X.; Kong, X.; Zhang, Y.; Rowsell, P.J.; Zhao, Z.; Huang, B.; Zhang, J. Late Miocene elevated horizontal karst caves and landform evolution as a response to tectonic uplift along with regional integration of fluvial drainage in southwestern China. *J. Earth Sci.* **2025**, *36*, 1717–1730. [CrossRef]
17. Audra, P.; Palmer, A.N. The pattern of caves: Controls of epigenic speleogenesis. *Géomorphologie Relief Process. Environ.* **2011**, *17*, 359–378. [CrossRef]
18. White, W.B. Geomorphology and Hydrology of Karst Terrains. 1988. Available online: https://digitalcommons.usf.edu/kip_articles/2160 (accessed on 26 June 2022).
19. Granger, D.E.; Fabel, D.; Palmer, A.N. Pliocene–Pleistocene incision of the Green River, Kentucky, determined from radioactive decay of cosmogenic 26Al and 10Be in Mammoth Cave sediments. *Geol. Soc. Am. Bull.* **2001**, *113*, 825–836. [CrossRef]
20. Worthington, S.R. Evolution of caves in response to base-level lowering. *Cave Karst Sci.* **2005**, *32*, 3–12.
21. Wagner, T.; Fritz, H.; Stüwe, K.; Nestroy, O.; Rodnight, H.; Hellstrom, J.; Benischke, R. Correlations of cave levels, stream terraces and planation surfaces along the River Mur—Timing of landscape evolution along the eastern margin of the Alps. *Geomorphology* **2011**, *134*, 62–78. [CrossRef]
22. White, W. Chemistry and karst. *Acta Carsologica* **2015**, *44*. [CrossRef]
23. Aley, T. Corrasional cave passage enlargement. *Cave Notes* **1965**, *7*, 2–4.
24. Sanders, W. Limestone Denudation. In *Karst Geomorphology: Benchmark Papers in Geology*; Sweeting, M., Ed.; Hutchinson Ross Publishing Company: Stroudsburg, PA, USA, 1981; Volume 59, pp. 320–343.
25. Bosch, R.F.; White, W.B. Lithofacies and Transport of Clastic Sediments in Karstic Aquifers. In *Studies of Cave Sediments*; Sasowsky, I.D., Mylroie, J., Eds.; Springer: Dordrecht, The Netherlands, 2007. [CrossRef]
26. Dogwiler, T.; Wicks, C.M. Sediment entrainment and transport in fluviokarst systems. *J. Hydrol.* **2004**, *295*, 163–172. [CrossRef]
27. Gutiérrez, F.; Parise, M.; De Waele, J.; Jourde, H. A review on natural and human-induced geohazards and impacts in karst. *Earth-Sci. Rev.* **2014**, *138*, 61–88. [CrossRef]
28. Girihagama, L.; Nof, D.; Hancock, C. Bubble-induced cave collapse. *PLoS ONE* **2015**, *10*, e0122349. [CrossRef]
29. Parise, M. A procedure for evaluating the susceptibility to natural and anthropogenic sinkholes. *Georisk Assess. Manag. Risk Eng. Syst. Geohazards* **2015**, *9*, 272–285. [CrossRef]
30. Perrotti, M.; Lollino, P.; Fazio, N.L.; Parise, M. Stability charts based on the finite element method for underground cavities in soft carbonate rocks: Validation through case-study applications. *Nat. Hazards Earth Syst. Sci.* **2019**, *19*, 2079–2095. [CrossRef]
31. Currens, J.C. *Kentucky Is Karst Country! What You Should Know About Sinkholes and Springs*; Technical Report Information Circular 4; Kentucky Geological Survey: Lexington, KY, USA, 2002. [CrossRef]
32. Palmer, A.N. Geomorphic interpretation of karst features. In *Groundwater as a Geomorphic Agent*; Routledge: London, UK, 2020; pp. 173–209.
33. Espinasa, L.; Borowsky, R. Eyed cave fish in a karst window. *J. Cave Karst Stud.* **2000**, *62*, 180–183.
34. Sauro, U. Closed depressions in karst areas. In *Encyclopedia of Caves*; White, W., Culver, D., Pipan, T., Eds.; Academic Press: San Diego, CA, USA, 2019; pp. 285–300.
35. White, E.L.; White, W.B. Karst landforms and drainage basin evolution in the Obey River basin, north-central Tennessee, USA. *J. Hydrol.* **1983**, *61*, 69–82. [CrossRef]
36. Woodside, J.; Peterson, E.W.; Dogwiler, T. Longitudinal profile and sediment mobility as geomorphic tools to interpret the history of a fluviokarst stream system. *Int. J. Speleol.* **2015**, *44*, 197–206. [CrossRef]
37. Jacoby, B.S.; Peterson, E.W.; Kostelnick, J.C.; Dogwiler, T. Approaching cave level identification with GIS: A case study of Carter Caves. *Int. Sch. Res. Not.* **2013**, *2013*, 160397. [CrossRef]
38. Engel, A.S.; Engel, S.E. A field guide for the karst of Carter Caves State Resort Park and the surrounding area, northeastern Kentucky. In *Select Field Guides to Cave and Karst Lands of the United States*; Karst Waters Institute: Lewisburg, PA, USA, 2009; Volume 15.
39. McGrain, P. *Geology of the Carter and Cascade Caves Area*; University of Kentucky: Lexington, KY, USA, 1954.
40. Ochsenbein, G. Origin of caves in Carter Caves State Park. Carter County, Kentucky. Master's Thesis, Bowling Green State University, Bowling Green, OH, USA, 1974.
41. Pfeffer, N.; Madigan, T.J.; Hobbs, H.H., III. Laurel Cave. *Pholeos* **1981**, *2*, 10–13.
42. Hobbs, H., III; Pender, M. The Horn Hollow Cave System. *Carter Cty. Ky. Pholeos* **1985**, *5*, 17–22.
43. Jacoby, B.S.; Peterson, E.W.; Dogwiler, T.; Kostelnick, J.C. Estimating the timing of cave level development with GIS. *Speleogenesis Evol. Karst Aquifers* **2011**, *11*, 52–61.
44. Angel, J.C.; Peterson, E.W. Nitrates in karst systems: Comparing impacted systems to a relatively unimpacted system. *J. Geogr. Geol.* **2015**, *7*, 65–76. [CrossRef]
45. Francis, A.K.; Peterson, E.W.; Dogwiler, T. Lithology as an erosional control on the Cave Branch and Horn Hollow fluviokarst watersheds in Carter County, Kentucky. In Proceedings of the 15th Multidisciplinary Conference on Sinkholes and the Engineering and Environmental Impacts of Karst, Shepherdstown, WV, USA, 2–6 April 2018. [CrossRef]

46. Kentucky Geological Survey. KGSGeoPortal: Gateway to Online Maps, Databases, and Publications for Kentucky. Available online: https://kgs.uky.edu/kgsmap/kgsgeoportal/kgsgeoportal.asp (accessed on 26 June 2022).
47. Slocum, T.A.; McMaster, R.M.; Kessler, F.C.; Howard, H.H.; Mc Master, R.B. *Thematic Cartography and Geographic Visualization*; CRC Press: Boca Raton, FL, USA, 2008.
48. Ford, D.; Williams, P.D. *Karst Hydrogeology and Geomorphology*; John Wiley & Sons: Hoboken, NJ, USA, 2007.
49. Jeffery, Z.E.; Penn, S.; Giles, D.P.; Hastewell, L. Identification, investigation and classification of surface depressions and chalk dissolution features using integrated LiDAR and geophysical methods. *Q. J. Eng. Geol. Hydrogeol.* **2020**, *53*, 620–644. [CrossRef]
50. Davis, W.M. Origin of limestone caverns. *Bull. Geol. Soc. Am.* **1930**, *41*, 475–628. [CrossRef]
51. Jakucs, L. Genetic types of the Hungarian karst. *Karszt Es Barlang Spec. Issue* **1977**, 3–18.
52. Bočić, N. Relation between karst and fluviokarst relief on the Slunj plateau (Croatia). *Acta Carsologica* **2003**, *32*, 137–146. [CrossRef]
53. Bogli, A. Corrosion par mélange des eaux. *Int. J. Speleol.* **1964**, *1*, 9. [CrossRef]
54. Wei, H.P.; Li, J.H.; Hu, W.; Li, R.Z.; Yu, D.B. Study on the identification of karst surface collapse via UAV photography based on the YOLO model. *Discov. Appl. Sci.* **2026**, *8*, 244. [CrossRef]

Disclaimer/Publisher's Note: The statements, opinions and data contained in all publications are solely those of the individual author(s) and contributor(s) and not of MDPI and/or the editor(s). MDPI and/or the editor(s) disclaim responsibility for any injury to people or property resulting from any ideas, methods, instructions or products referred to in the content.